

A Prolate-Element Method for Nonlinear PDEs on the Sphere

Jing Zhang · Li-Lian Wang · Zhijian Rong

Received: 2 March 2010 / Revised: 25 August 2010 / Accepted: 9 September 2010
© Springer Science+Business Media, LLC 2010

Abstract A p -type spectral-element method using prolate spheroidal wave functions (PSWFs) as basis functions, termed as the prolate-element method, is developed for solving partial differential equations (PDEs) on the sphere. The gridding on the sphere is based on a projection of the prolate-Gauss-Lobatto points by using the cube-sphere transform, which is free of singularity and leads to quasi-uniform grids. Various numerical results demonstrate that the proposed prolate-element method enjoys some remarkable advantages over the polynomial-based element method: (i) it can significantly relax the time step size constraint of an explicit time-marching scheme, and (ii) it can increase the accuracy and enhance the resolution.

Keywords Bandlimited basis · Prolate-Gauss-Lobatto points · Cube-sphere transform · Spectral-element method · Quasi-uniform grids

1 Introduction

Spectral method has become fairly attractive for simulations with stringent accuracy and/or memory requirements (cf. [3, 8, 9]). Over the past two decades, it has dominated the area of weather prediction and climate modeling. Indeed, in the 1990s, the spectral transform method based on the spherical harmonics has been extensively used (cf. [3, 14] and the references therein), after all the spherical harmonics are the eigenfunctions of the Laplace operator. However, this global method makes use of highly non-uniform computational grids,

This work is partially supported by Singapore AcRF Tier 1 Grant RG58/08, Singapore MOE Grant T207B2202, and Singapore NRF2007IDM-IDM002-010.
The work of the second author is also partially supported by a Leading Academic Discipline Project of Shanghai Municipal Education Commission, China (No. J50101).

J. Zhang · L.-L. Wang (✉)
Division of Mathematical Sciences, School of Physical and Mathematical Sciences,
Nanyang Technological University, Singapore 637371, Singapore
e-mail: LiLian@ntu.edu.sg

Z. Rong
School of Mathematical Sciences, Xiamen University, Xiamen 361005, China

requires expensive nonlocal communication operations and has difficulty in exploiting high-performance parallel computing. The local spectral-element method can overcome these deficiencies, so it has attracted many attentions since 1990s (see, e.g., [14, 18, 27, 40, 41]). One major type of elements is based on the cube-sphere partition of the sphere (introduced by Sadourny [33] and further developed by [24, 32, 40]). As pointed out in [32], the cube-sphere transform meets the desirable features for a “good” partition proposed by Phillips [29]. However, the direct projection of the Legendre-Gauss-Lobatto (LGL) points by this transform still leads to unsatisfactory grid distributions (see Fig. 4 (right) below), as the grid points are much denser near boundaries of the elements and the non-uniformity is even severer when each patch is partitioned into many more elements. Consequently, the explicit time discretization suffers from the Courant-Friedrichs-Lewy (CFL) condition so the time step has to be very small for a stable computation. To overcome this difficulty, some semi-implicit and fully implicit schemes were proposed in e.g., [41, 49]. However, this requires robust solvers for the resultant systems which normally involve a huge number of unknowns (cf. [23]), so many efforts need to be devoted to constructing a suitable preconditioning (cf. [42]).

In this paper, we propose a p -type element method based on the cube-sphere projection of the prolate-Gauss-Lobatto points generated from the prolate spheroidal wave functions (PSWFs). This leads to almost uniform computational grids on the sphere (see Fig. 4 (middle) below), so it can significantly relax the CFL constraint and the time step limitation. Typically, various numerical experiments indicate that with a suitable choice of the bandwidth parameter, the proposed method can achieve a nearly $O(N^{-1})$ time step restriction by using N^2 points on each patch. It is worthwhile to point out that Kosloff and Tal-Ezer [19] proposed a mapped spectral method to obtain an $O(N^{-1})$ Runge-Kutta method for first-order problems. In fact, a composition of the cube-sphere transform and the mapping in [19] can also produce almost uniform grids on the sphere. However, the error estimates in [36] indicate that the accuracy is deteriorated when the parameter suggested in [19] is chosen. On the other hand, the presence of the extra mapping complicates the original problem. In contrast, the PSWF-based method uses a natural set of Gauss-type points and can be easily extended from the usual spectral-element method. Moreover, the prolate-element method inherits some other advantages over the polynomial-based approaches, that is, the gain in accuracy and in enhancement of resolution. These merits have also been observed and/or analyzed for PSWF-based spectral methods (cf. [2, 5, 10, 20, 45]).

The rest of the paper is organized as follows. In the next section, we review some basic properties of the PSWFs. In Sect. 3, we first introduce the cube-sphere transform, and then develop the prolate-element methods based on a collocation formulation for advection transport on the sphere. Finally, we apply this p -type method to reaction-diffusion models for texture synthesis and the fourth-order Cahn-Hilliard equation for phase transition on the sphere. Moreover, we present ample numerical results for each application in Sect. 3 to demonstrate the advantages of the proposed method. We conclude the paper with some remarks.

2 Prolate Spheroidal Wave Functions

We collect in this section some relevant properties of the PSWFs, and introduce the associated quadrature and interpolation.

2.1 Basic Properties

The PSWFs, denoted by $\psi_n^c(x)$, are eigenfunctions of the Sturm-Liouville problem:

$$D_x \psi_n^c := -\partial_x((1-x^2)\partial_x \psi_n^c) + c^2 x^2 \psi_n^c = \chi_n^c \psi_n^c, \quad x \in I := (-1, 1), \quad c \geq 0, \tag{2.1}$$

where $\{\chi_n^c\}$ are the corresponding eigenvalues, and the constant c is called the *bandwidth parameter*. In particular, if $c = 0$, the PSWFs are reduced to the classical Legendre polynomials and the eigenvalues $\chi_n^0 = n(n+1)$.

The following properties, which are typical for eigenfunctions of Sturm-Liouville equations (cf. [1, 11]), can be found in, e.g., [13, 21, 25, 38, 39, 48]. More precisely, for any $c > 0$, we have

- (i) $\{\psi_n^c\}_{n=0}^\infty$ are smooth and form a complete orthonormal system of $L^2(I)$, namely,

$$\int_{-1}^1 \psi_m^c(x) \psi_n^c(x) dx = \delta_{mn}, \tag{2.2}$$

where δ_{mn} is the Kronecker delta.

- (ii) $\{\chi_n^c\}_{n=0}^\infty$ are real, positive, simple and ordered as

$$0 < \chi_0^c < \chi_1^c < \dots < \chi_n^c < \dots \tag{2.3}$$

Moreover, there holds the estimate (cf. [45]):

$$n(n+1) < \chi_n^c < n(n+1) + c^2. \tag{2.4}$$

- (iii) $\{\psi_n^c\}_{n=0}^\infty$ are even (resp. odd) for even (resp. odd) n , that is,

$$\psi_n^c(-x) = (-1)^n \psi_n^c(x), \quad \forall x \in I. \tag{2.5}$$

- (iv) ψ_n^c has exactly n real distinct zeros in the interval $(-1, 1)$.

As a remarkable coincidence, the PSWFs are also eigenfunctions of an integral operator (cf. [39]):

$$i^n \lambda_n^c \psi_n^c(x) = \int_{-1}^1 e^{icxt} \psi_n^c(t) dt, \quad \forall x \in (-1, 1), \quad \forall c > 0, \tag{2.6}$$

where the corresponding eigenvalues $\{\lambda_n^c\}$ (modulo the factor i^n) are all real, positive, simple and of the ordering

$$\lambda_0^c > \lambda_1^c > \dots > \lambda_n^c > \dots > 0, \quad \forall c > 0. \tag{2.7}$$

Thanks to the notable property (2.6), the PSWFs are bandlimited in frequency domain and mostly concentrated in time domain. Moreover, They form an optimal basis for approximating bandlimited functions (see, e.g., [21, 37, 39]).

Compared with the Legendre polynomials, the PSWFs oscillate more uniformly. In Fig. 1, we plot some samples with various c , and see that the zeros of ψ_n^c become more uniformly distributed as c increases. Indeed, they behave like (cf. [4]):

$$\psi_n^c(x) \sim \sqrt{\frac{2}{\pi}} \frac{1}{c} \frac{1}{\sqrt{1-x^2}} \cos([\pi/2]n(1-x)) \quad \text{for } c = c_*(n) = \frac{\pi}{2} \left(n + \frac{1}{2}\right), \quad n \gg 1, \tag{2.8}$$



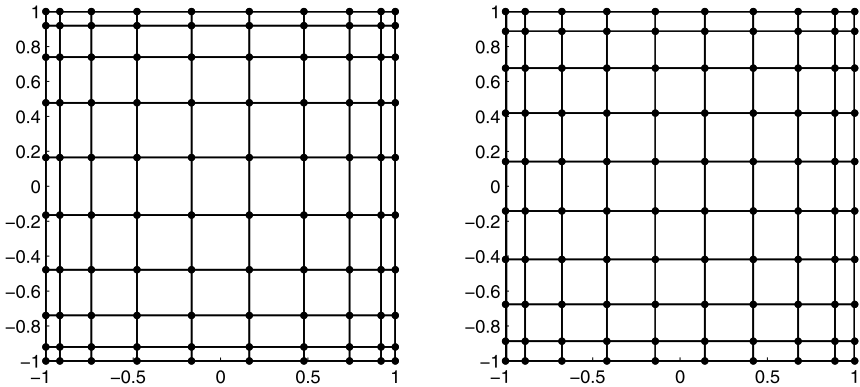


Fig. 2 Distribution of 10×10 tensorial prolate-Gauss-Lobatto points with $c = 0$ (left) and $c = 8$ (right)

Define the finite dimensional space

$$X_N^c = \text{span}\{\psi_n^c(x) : 0 \leq n \leq N\}. \tag{2.12}$$

As a generalization of the polynomial interpolation, the PSWF interpolation $I_N^c : C[-1, 1] \rightarrow X_N^c$, is defined by

$$I_N^c u \in X_N^c \text{ and } u(x_j^c) = (I_N^c u)(x_j^c), \quad 0 \leq j \leq N. \tag{2.13}$$

Correspondingly, we introduce the Lagrange-type nodal basis of the form

$$h_j^c(x) = \sum_{k=0}^N d_k^j \psi_k^c(x) \in X_N^c, \quad 0 \leq j \leq N, \tag{2.14}$$

where the coefficients $\{d_k^j\}$ are uniquely determined by the interpolating condition:

$$h_j^c(x_i^c) = \delta_{ij}, \quad 0 \leq i, j \leq N. \tag{2.15}$$

Accordingly, we can introduce the differentiation matrices in the same fashion as the Legendre and Chebyshev spectral methods (see, e.g., [8, 16]).

3 Prolate-Element Method on the Sphere

The section is devoted to introducing the p -type prolate-element method on the sphere using PSWFs as basis functions. The computational grids are generated by a cubed-sphere projection (cf. [33]) of the prolate-Gauss-Lobatto points, so the partition is free of singularity and the grid points are quasi-uniformly distributed. As some applications, the proposed method will be applied to the advection flow, reaction-diffusion models for texture synthesis, and the Cahn-Hilliard equation for phase transition on the sphere.

3.1 Cubed-Sphere Transform

The cubed-sphere transform was originally introduced by Sadourny [33] (and further developed by [24, 32, 40]), to overcome the pole singularity induced by the spherical transform. The basic idea is to partition the sphere into six identical patches through a central projection of the faces of the inscribed cube onto the spherical surface so that each of the six local coordinates is free of singularity. More precisely, let (X, Y, Z) be the Cartesian coordinate on the sphere

$$S := S_R := \left\{ (X, Y, Z) \in \mathbb{R}^3 : X^2 + Y^2 + Z^2 = R^2 \right\}, \tag{3.1}$$

and let Q be the inscribed cube centered at origin with faces perpendicular to the axes. Note that the length of each size of Q is $2a = 2R/\sqrt{3}$. As illustrated in Fig. 3, the so-called gnomonic projection (from the origin) projects the faces of Q onto S , which decomposes S into six identical patches. Here, we label the four patches along the equator by $P_n, n = 1, 2, 3, 4$, and the top (or north-pole) and the bottom (or the south-pole) patches by P_5 and P_6 , respectively. Note that the corresponding faces of Q are also labeled by $\{P_n\}_{n=1}^6$ accordingly, see Fig. 3 (right).

Let (x, y) be the local coordinate on Q . One finds the transform between S and Q :

$$(X, Y, Z) = \frac{R}{r} \begin{cases} (a, x, y), & \text{on } P_1, \\ (-x, a, y), & \text{on } P_2, \\ (-a, -x, y), & \text{on } P_3, \\ (x, -a, y), & \text{on } P_4, \\ (-y, x, a), & \text{on } P_5, \\ (y, x, -a), & \text{on } P_6, \end{cases} \quad (x, y) = a \begin{cases} (Y/X, Z/X), & \text{on } P_1, \\ (-X/Y, Z/Y), & \text{on } P_2, \\ (Y/X, -Z/X), & \text{on } P_3, \\ (-X/Y, -Z/Y), & \text{on } P_4, \\ (Y/Z, -X/Z), & \text{on } P_5, \\ (-Y/Z, -X/Z), & \text{on } P_6, \end{cases} \tag{3.2}$$

where $r = \sqrt{a^2 + x^2 + y^2}$. It is referred to as the equidistant central projection (see Fig. 4 (left) for the distribution of the prolate-Gauss-Lobatto points via this transform).

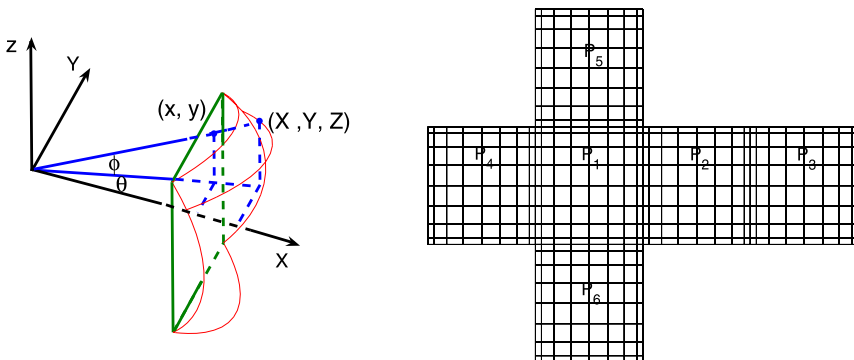


Fig. 3 Left: schematic illustration of the gnomonic (central) projection between the sphere of radius R and the inscribed cube with side of length $2a$. Right: the prolate points with $N = 9$ and $c = 8$ on the (expanded) six faces of the cube

To obtain more uniform computational grids, we use a second mapping as suggested in [31]:

$$x = a \tan \frac{\pi \xi}{4}, \quad y = a \tan \frac{\pi \eta}{4}, \quad \forall \xi, \eta \in [-1, 1]. \tag{3.3}$$

This defines (ξ, η) -coordinate on the reference square $(-1, 1)^2$, and we have the relation:

$$(\xi, \eta) = \frac{4}{\pi} \arctan \begin{cases} (Y/X, Z/X), & \text{on } P_1, \\ (-X/Y, Z/Y), & \text{on } P_2, \\ (Y/X, -Z/X), & \text{on } P_3, \\ (-X/Y, -Z/Y), & \text{on } P_4, \\ (Y/Z, -X/Z), & \text{on } P_5, \\ (-Y/Z, -X/Z), & \text{on } P_6. \end{cases} \tag{3.4}$$

In Fig. 4 (middle and right), we compare the grid distribution through the equiangular central projection of the prolate-Gauss-Lobatto and Legendre-Gauss-Lobatto in Fig. 2, and find that the mapped prolate-Gauss-Lobatto points are almost uniformly distributed on the sphere. It is anticipated that the prolate-element methods can significantly relax the constraint of explicit time stepping and enhance the spatial resolution, which will be demonstrated below.

In what follows, we use the spherical transform (i.e., the longitude and latitude coordinate (θ, ϕ)) as an intermediate coordinate system:

$$X = R \cos \theta \cos \phi, \quad Y = R \sin \theta \cos \phi, \quad Z = R \sin \phi, \tag{3.5}$$

where we take $\phi \in [-\pi/2, \pi/2]$ and $\theta \in [-\pi/4, 7\pi/4]$. One finds that (cf. Fig. 3 (left)) the angular variable θ of the four patches $P_1 - P_4$ along the equator has the range:

$$\theta \in \Theta_k := [-\pi/4, \pi/4] + (k - 1)\pi/2, \quad 1 \leq k \leq 4. \tag{3.6}$$

We present in Appendix the basic calculus of the common differential operators expressed in a general curvilinear coordinate, and make it specific for the aforementioned three coordinates, i.e., (x, y) , (ξ, η) and (ϕ, θ) .

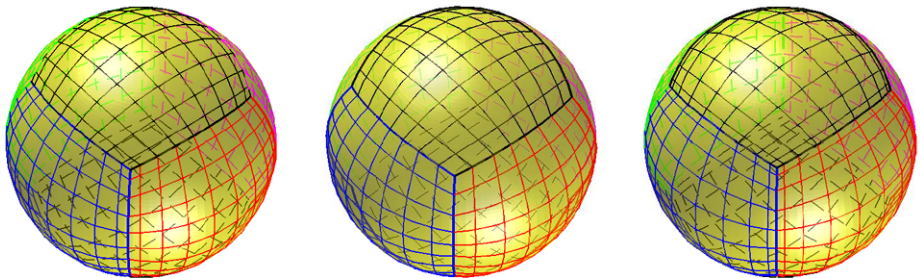


Fig. 4 The grid distribution on the sphere with 10×10 points on each patch. *Left:* (x, y) to (X, Y, Z) with $c = 8$. *Middle:* (ξ, η) to (X, Y, Z) with $c = 8$. *Right:* (ξ, η) to (X, Y, Z) with $c = 0$

3.2 Advection Transport on the Sphere

Consider the conservative transport on the sphere governed by the continuity equation in flux form (see, e.g., [27]):

$$\frac{\partial \Phi}{\partial t} + \operatorname{div}(\Phi \mathbf{V}) = 0 \quad \text{on } S \times (0, T]; \quad \Phi|_{t=0} = \tilde{\Phi}_0, \tag{3.7}$$

where Φ is the advection field and $\mathbf{V} = (u, v)'$ is the horizontal wind vector. To this end, S is a unit sphere. The equation (3.7) can be formulated in any curvilinear coordinate in a uniform format (see Appendix). With a little abuse of notation, we denote the transformed functions by the same notation as for the original ones throughout the paper.

Computationally, it is more suitable to use the form in (ξ, η) -coordinate system defined in (3.2)–(3.3) (cf. (A.7)):

$$\frac{\partial(\sqrt{g}\Phi)}{\partial t} + \frac{\partial(\sqrt{g}v^1\Phi)}{\partial \xi} + \frac{\partial(\sqrt{g}v^2\Phi)}{\partial \eta} = 0, \tag{3.8}$$

where \sqrt{g} is the Jacobian of the Cartesian coordinate (X, Y, Z) to (ξ, η) given by (A.11). The contravariant components v^1 and v^2 are determined by \mathbf{V} (cf. Formula (32) and Appendix B of [27]).

Next, we describe the prolate-element scheme based on a collocation formulation for (3.7). As in Sect. 3.1, we partition S into six identical (closed) patches $\{P_n\}_{n=1}^6$, i.e., $S = \bigcup_{n=1}^6 P_n$. Let $\Lambda = [-1, 1]^2$ be the reference square, and denote the mapping from Λ to P_n by $\mathcal{F}_n : \Lambda \rightarrow S$, which is a composition of (3.2) and (3.3). Let $\{x_j^c, \omega_j^c\}_{j=0}^N$ be the prolate-Gauss-Lobatto points and weights defined in (2.9)–(2.10), and let $\{h_j^c\}_{j=0}^N$ be the nodal basis in (2.14). Define the finite dimensional space

$$Y_N^c = \operatorname{span}\{h_i^c(\xi)h_j^c(\eta) : 0 \leq i, j \leq N, (\xi, \eta) \in \Lambda\}. \tag{3.9}$$

The prolate-element approximation of (3.7) in collocation formulation is to find Φ_N on the sphere such that

- Φ_N is continuous across the patches;
- For each of the six patches, we seek $\Phi_n := \Phi_N \circ \mathcal{F}_n|_{(\xi, \eta) \in \Lambda} \in Y_N^c$, such that

$$\left(\frac{\partial \Phi_n}{\partial t} + L(\Phi_n)\right)\Big|_{(\xi, \eta) = (x_i^c, x_j^c)} = 0, \quad 0 \leq i, j \leq N, \quad 1 \leq n \leq 6, \tag{3.10}$$

where

$$L(\varphi) = \frac{1}{\sqrt{g}} \left(\frac{\partial(\sqrt{g}v^1\varphi)}{\partial \xi} + \frac{\partial(\sqrt{g}v^2\varphi)}{\partial \eta} \right). \tag{3.11}$$

The subproblems in (3.10) can be discretized in time by various schemes (see, e.g., [27, 49]). To show the effect of the quasi-uniform grids, we intend to adopt the explicit third-order Adams-Bashforth scheme of the form

$$\Phi_n^{k+3} = \Phi_n^{k+2} + \frac{\tau}{12} (23L(\Phi_n^{k+2}) - 16L(\Phi_n^{k+1}) + 5L(\Phi_n^k)), \quad 1 \leq n \leq 6, \tag{3.12}$$

where τ is the time step size, and Φ_n^k is the approximation of Φ_n at $t = k\tau$ for $0 \leq k \leq [T/\tau] - 3$. We use a one-step scheme such as the third-order Runge-Kutta method to generate the initial values Φ_n^1 and Φ_n^2 from given Φ_n^0 . In short, at each iteration, we update Φ_N on

the reference domain Λ for each patch by evaluating (3.12) locally, and assemble new Φ_N modifying the values Φ_n at the boundaries of P_n to ensure continuity across the elements as usual.

We test the deformation flow (cf. [26, 27]) consisting of two opposite vortices located at two poles of the rotated spherical coordinates (θ', ϕ') , which has the north pole (θ_0, ϕ_0) with respect to the regular spherical coordinate system (θ, ϕ) in (3.5). For any given position of the north pole (θ_0, ϕ_0) , the rotated coordinate (θ', ϕ') is computed from (θ, ϕ) by

$$\begin{cases} \theta' = \arctan\left(\frac{\cos \phi \sin(\theta - \theta_0)}{\cos \phi \sin \phi_0 \cos(\theta - \theta_0) - \cos \phi_0 \sin \phi}\right), \\ \phi' = \arcsin\left(\sin \phi \sin \phi_0 + \cos \phi \cos \phi_0 \cos(\theta - \theta_0)\right). \end{cases} \tag{3.13}$$

Define the horizontal wind velocity $V = (u, v)'$ in (3.7) as

$$\begin{cases} u = \omega'(\phi')(\sin \phi_0 \cos \phi - \cos \phi_0 \cos(\theta - \theta_0) \sin \phi), \\ v = \omega'(\phi') \cos \phi_0 \sin(\theta - \theta_0), \end{cases} \tag{3.14}$$

where

$$\omega'(\phi') = \begin{cases} 0, & \text{if } \rho' = 0, \\ \frac{3\sqrt{3} \operatorname{sech}^2 \rho' \tanh \rho'}{2\rho'}, & \text{if } \rho' \neq 0, \end{cases}$$

with $\rho' = \mu \cos \phi'$ and μ being a constant. With the input (3.14), the equation (3.7) admits the exact solution

$$\Phi(\theta', \phi', t) = 1 - \tanh\left(\frac{\rho'}{\nu} \sin(\theta' - \omega' t)\right), \tag{3.15}$$

where ν is a nonzero constant. In the following computations, we take $\mu = 3, \nu = 5$, and the initial value $\tilde{\Phi}_0 = \Phi(\theta', \phi', 0)$.

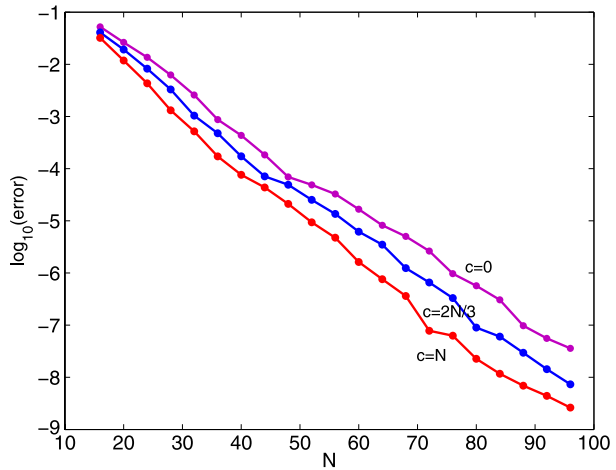
In the first test, we particularly choose $(\theta_0, \phi_0) = (0, \pi/2)$ so that two vortices symmetrically locate at two poles of the sphere. This appears to be an ideal problem to examine the effect of uniformity of the grids.

In Table 1, we tabulate the maximum point-wise errors at $t = 3$ for various choices of c, N and τ . Observe from Table 1(a) that compared with the usual polynomial-based element method (i.e., $c = 0$), the prolate-element method with $c = N$ requires about ten times fewer steps to achieve even better accuracy in the last column. In Table 1(b), we present the maximum point-wise errors for $c = N$. It shows that the proposed method on quasi-uniform grids can significantly relax the time step size. Indeed, the scheme with $c = N$ is

Table 1 Convergence of the prolate-element method for deformation flow on the sphere

N	c	Steps	Error	N	τ	Error
64	0	12288	8.13E-06	64	$64^{-0.9}$	2.11E-02
72	0	15552	2.62E-06	72	$72^{-0.9}$	4.70E+02
80	0	19200	5.56E-07	80	$80^{-0.9}$	2.37E+07
64	64	1536	7.60E-07	64	64^{-1}	7.12E-06
72	72	1500	8.27E-08	72	72^{-1}	4.98E-06
80	80	1000	6.58E-08	80	80^{-1}	6.58E-08

Fig. 5 The maximum point-wise errors at $t = 3$ against N for $c = 0, 2N/3, N$ and $\tau = N^{-3/2}$



stable for $\tau = O(N^{-1})$ (but not stable for $\tau = O(N^{-0.9})$), rather than $O(N^{-2})$ for the usual Legendre-Gauss-Lobatto based element method (cf. [8]).

In Fig. 5, we plot the maximum point-wise error against N for $\tau = N^{-3/2}$ and $c = 0, 2N/3, N$, which shows that the choice of $c = 2N/3, N$ leads to more accurate numerical solutions. In other words, a larger time step can be adopted.

Next, we apply the proposed method to simulate the deformation flow up to $t = 10$ with vortex center $(\theta_0, \phi_0) = (0, \pi/2), (\pi - 0.8, \pi/4.8)$, where in the latter case, two opposite vortices are located at two common vertices of three patches (P_2, P_3, P_5) and (P_1, P_4, P_6) , respectively. Notice that as time evolves, thinner and thinner vortex layers are emerged. In Fig. 6(a)–(d), we depict numerical solutions at $t = 10$ for both cases, and plot their graphs on P_5 in Fig. 6(e)–(f). Here, the maximum point-wise errors at $t = 10$ for two tests are about 10^{-4} .

3.3 Reaction-Diffusion Models for Texture Synthesis

Texture synthesis is one fundamental task in computer vision. One important approach is to generate texture by simulating a process of local nonlinear reaction diffusion, which is capable of overcoming the distortions induced by the commonly used texture mappings (see, e.g., [46, 47]).

3.3.1 Gray-Scott's Model

We consider the model with isotropic diffusion:

$$\frac{\partial a}{\partial t} = d_a \Delta a + F(a, b), \quad \frac{\partial b}{\partial t} = d_b \Delta b + G(a, b), \quad \text{on } S \times (0, T], \quad (3.16)$$

where a and b are concentrations of two “chemicals”, d_a and d_b are the diffusion rates of a and b , respectively, and F and G are the reaction terms. Various F and G have been used, among which the classical but popular one is known as the Turing model [43], and an interesting variant has been discussed in e.g., [17, 46]. Here, we consider the Gray-Scott's model [17, 35]:

$$F(a, b) = s(\alpha - a + a^2b), \quad G(a, b) = s(\beta - a^2b), \quad (3.17)$$

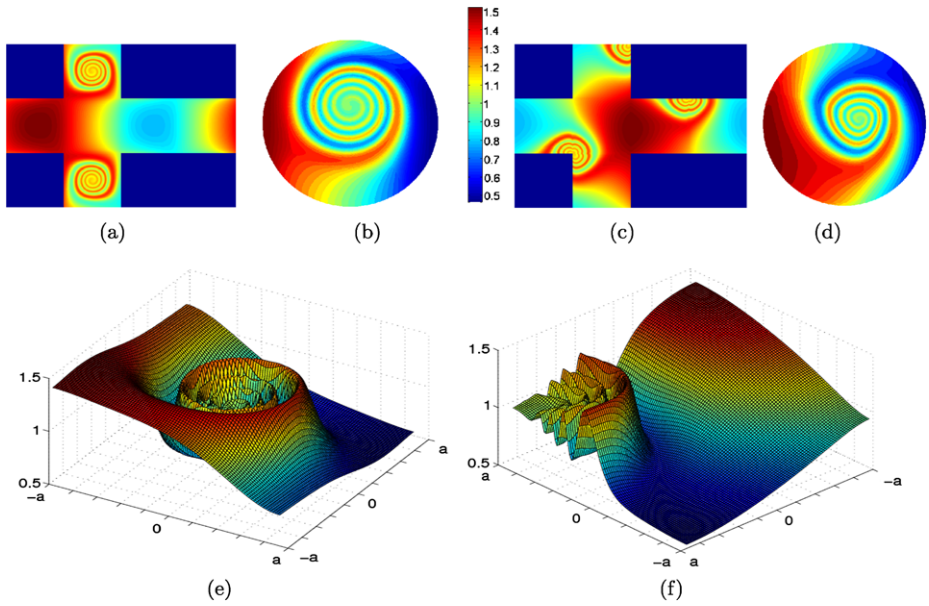


Fig. 6 Numerical vortices on the cubed faces and spherical surfaces at $t = 10$ computed by (3.12) with $N = 96, c = N/2$ and $\tau = N^{-3/2}$, where the vortex center: $(\theta_0, \phi_0) = (0, \pi/2)$ for (a)–(b), and $(\theta_0, \phi_0) = (\pi - 0.8, \pi/4.8)$ for (c)–(d). The second row is the numerical structure of the vortices on patch P_5 for vortex center at $(0, \pi/2)$ (e) and $(\pi - 0.8, \pi/4.8)$ (f), respectively

where s is the reaction rate, and α, β are two constants.

Let τ be the time step, and let (a^k, b^k) be the approximation of (a, b) at $t = k\tau$ for $k = 1, \dots, [T/\tau]$. We discretize (3.16)–(3.17) in time by using Crank-Nicolson-leap-frog scheme:

$$\begin{cases} \frac{a^{k+1} - a^{k-1}}{2\tau} = d_a \Delta \left(\frac{a^{k+1} + a^{k-1}}{2} \right) + F(a^k, b^k), \\ \frac{b^{k+1} - b^{k-1}}{2\tau} = d_b \Delta \left(\frac{b^{k+1} + b^{k-1}}{2} \right) + G(a^k, b^k). \end{cases} \quad (3.18)$$

Setting

$$u_1 = \frac{a^{k+1} + a^{k-1}}{2}, \quad u_2 = \frac{b^{k+1} + b^{k-1}}{2},$$

we find that at each time step we need to solve two elliptic equations:

$$-\tau d_a \Delta u_i + u_i = f_i \quad \text{on } S, \quad i = 1, 2, \quad (3.19)$$

where $f_1 = a^{k-1} + \tau F(a^k, b^k)$ and $f_2 = b^{k-1} + \tau G(a^k, b^k)$. Hence, it is necessary to develop the prolate-element solver for elliptic equations.

3.3.2 Prolate-Element Solver for Elliptic Equations

Consider

$$-\text{div}(A\nabla u) + Bu = f \quad \text{on } S, \quad (3.20)$$

where A, B and f are given functions such that (3.20) is elliptic. The standard Galerkin formulation for (3.20) is to find $u \in H^1(S)$ such that

$$(A \nabla u, \nabla v) + (Bu, v) = (f, v), \quad \forall v \in H^1(S), \tag{3.21}$$

which has a unique solution if $f \in L^2(S)$. As before, we partition S into six identical patches $\{P_n\}_{n=1}^6$ (can be viewed as curved p -elements), which are the images of the reference square $\Lambda = [-1, 1]^2$ under the corresponding mapping $\{\mathcal{F}_n\}_{n=1}^6$. The associated transformed differential operators are formulated in Appendix. Hence, by swapping the polynomial nodal basis and the Legendre-Gauss-Lobatto quadratures respectively with (3.9) and

$$(u, v)_N = \sum_{i,j=0}^N u(\xi_i^c, \eta_j^c) v(\xi_i^c, \eta_j^c) \omega_i^c \omega_j^c, \quad \forall u, v \in C(\Lambda), \tag{3.22}$$

where $\{(\xi_i^c, \eta_j^c) = (x_i^c, x_j^c)\}$ and $\{\omega_i^c\}$ are given in (2.9)–(2.10), the C^0 -prolate-element method for (3.21) can be implemented as the usual C^0 -Legendre-spectral-element method (cf. [9, 12, 28]). Notice that the mappings \mathcal{F}_n are nonlinear, but are free of singularity. Here, we use the iteration solver, the bi-conjugated gradient stabilized (BICGSTAB) method, to solve the resultant system.

We test the scheme for solving (3.20) with four different sets of coefficients A, B and exact solution u on the unit sphere S (see the caption of Fig. 7). In Fig. 7, we plot \log_{10} of the maximum point-wise errors against N with several typical choices of bandwidth parameter c . We see that the method with $c < N$ provides more accurate approximations. Indeed, Chen et al. [10] empirically suggested the choice of $c = N/2$ in the one-dimensional case. We also observe that in all cases, the choice of $c = N/2$ seems to be more desirable. In fact, a very similar convergence behavior was also observed for the prolate-Galerkin approach in a single two-dimensional domain (see Fig. 5 in [45]). In particular, we point out that given the test solution in Fig. 7(c), the choice of $c = 10\pi$ should be the best, since it is expected to have a super-geometric convergence (cf. Theorem 3.1 in [45]).

We remark that by using the approximation results in [45], the Galerkin formulation can be analyzed in a similar fashion as the usual spectral-element method. However, to the best of our knowledge, the results on the prolate-Gauss-Lobatto interpolation errors are not available, so the analysis of the Galerkin scheme with numerical integration might not be possible without the aid of these results.

3.3.3 Numerical Results for (3.18)–(3.19)

With the above preparation, we solve (3.19) by using the foregoing elliptic solver. We first test the proposed method for three sets of parameters and initial conditions: (i) $\tau = 10^{-4}$, $N = 48$ and $s = 200$; (ii) $\tau = 10^{-2}$, $N = 32$ and $s = 50$; (iii) $\tau = 10^{-2}$, $N = 48$ and $s = 50$, and choose the following common parameters

$$d_a = 0.05, \quad d_b = 1, \quad \alpha = 0.1305, \quad \beta = 0.7695, \quad R = 1, \quad c = N/2.$$

In all three tests, the initial values are $b_0 \equiv 0.95$ and $a_0 = 0.9$ with a small Gaussian perturbation at the common vertices of P_1, P_2 and P_5 (with an additional Gaussian perturbation at the opposite vertex for Test (iii)) of magnitude 10^{-3} and different “radius” of the “support”.

In Fig. 8, we plot the patterns (a -component) at different time of the reaction-diffusion process on the sphere and cube faces in three tests. Due to the competition of reaction and

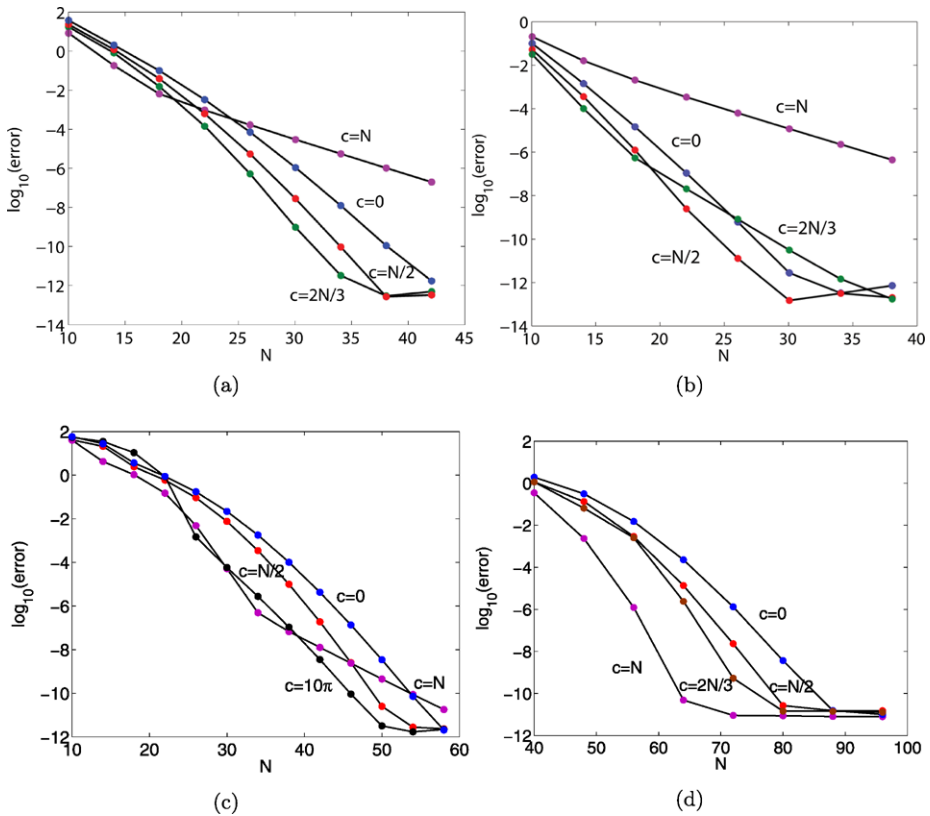


Fig. 7 \log_{10} of the maximum point-wise errors against N with various bandwidth parameter c . In (a), $A = 1, B = 2$ and $u = (X - 2)^2 \exp(4YZ) \sin(5\pi X)$. In (b), $A = 2 + \sin X, B = 1$ and $u = (X - 2)^2 \exp(3YZ) \sin(2\pi X)$. In (c), $A = B = 1$ and $u = \sin(10\pi Y)$. In (d), $A = B = 1$, and $u = \exp(3YZ) \sin(20\pi Y)$

diffusion, the initial perturbation is amplified and spread that leads to different patterns such as spots and stripes. Although these patterns are typical for the Turing model (see, e.g., [44]), their synthesis is sensitive to the choices of parameters, initial inputs, geometry of the computational domain and/or the accuracy of the numerical approaches (cf. [50]). It is interesting to see some new patterns generated by the Gray-Scott’s model by using the proposed high-order methods.

Similar to the Turing model (cf. [34] for analysis), the reaction rate s also controls the size of the patterns. As an illustration, we vary s in Test (i) and plot in Fig. 9 the final stable patterns for different s , which shows that the size of the spots becomes larger as s gets smaller.

3.4 Cahn-Hilliard Equation

As the last example, we consider the Cahn-Hilliard equation (cf. [7]):

$$\frac{\partial u}{\partial t} = \Delta(-\varepsilon^2 \Delta u + f(u)) \quad \text{on } S \times (0, T]; \quad u|_{t=0} = u_0 \quad \text{on } S, \quad (3.23)$$

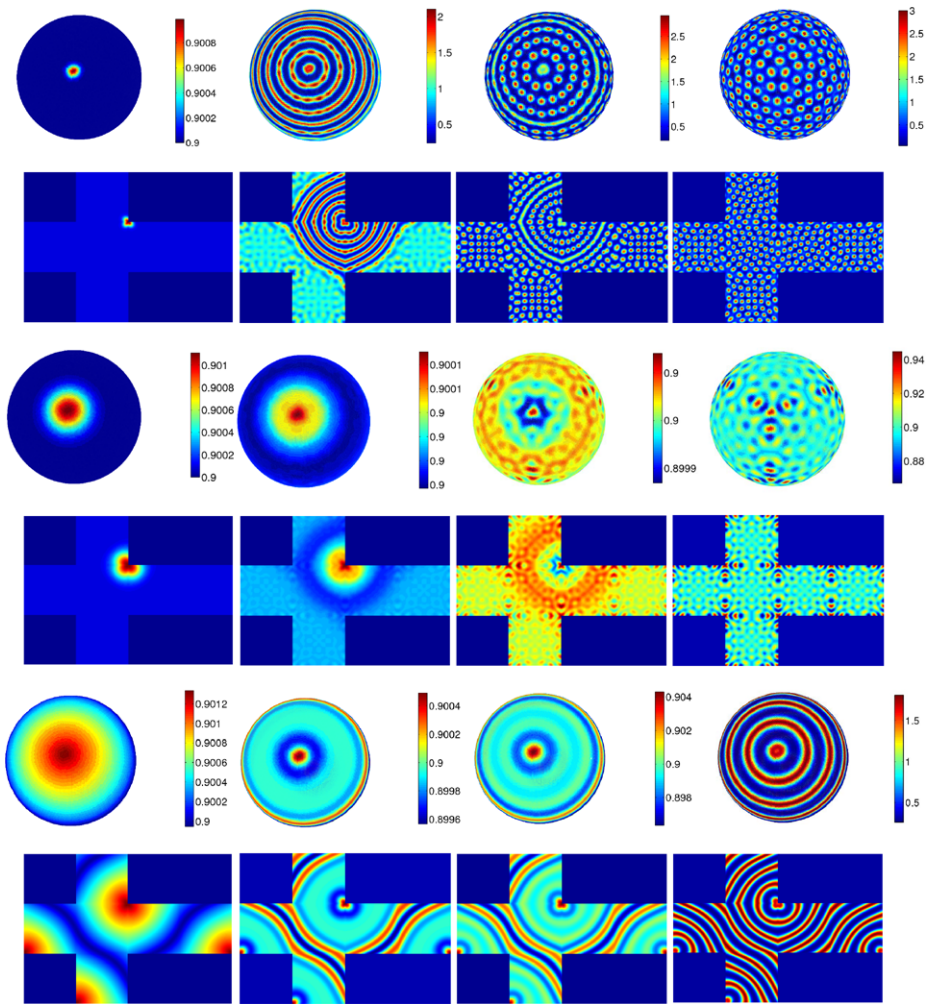


Fig. 8 Patterns synthesized by the reaction-diffusion model (3.16)–(3.17) on the spherical surfaces and the inscribed cube faces. Three tests are depicted: rows 1–2 for Test (i) at $t = 0, 0.37, 0.53, 3.87$; rows 3–4 for Test (ii) at $t = 0, 0.15, 0.2, 0.35$; and rows 5–6 for Test (iii) at $t = 0, 0.2, 0.4, 1.1$, respectively

where $\varepsilon > 0$ and $f(u) = u^3 - u$. It is a classical phase field model for spinodal decomposition of alloys, which involves the coarsening dynamics such as the process of phase separation following a quench from a disordered to an ordered phase.

Define the energy

$$E(u) = \int_S \left(\frac{\varepsilon^2}{2} |\nabla u|^2 + F(u) \right) dS, \tag{3.24}$$

where $F'(u) = f(u)$, namely,

$$F(u) = \frac{u^4}{4} - \frac{u^2}{2}.$$

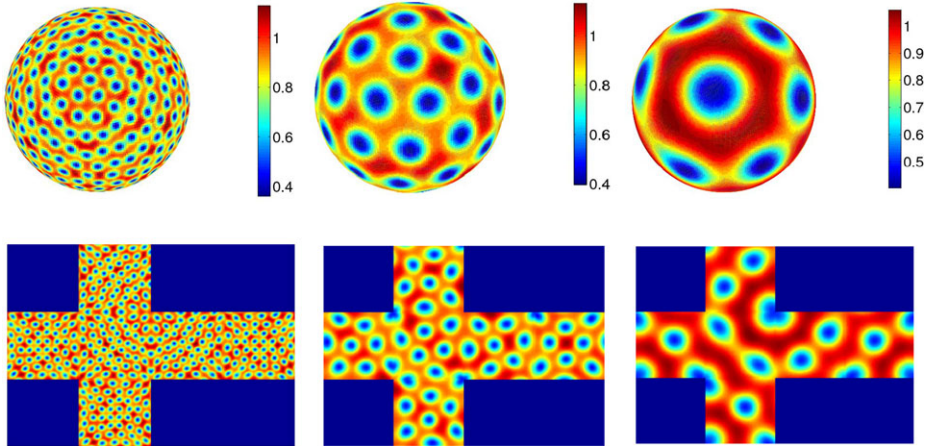


Fig. 9 Patterns for different reaction rate s . From left to right: $s = 50, 30, 10$ and $t = 3.87, 12, 12$, respectively

One verifies readily that

$$\frac{\partial E}{\partial t} = - \int_S |\nabla(-\varepsilon^2 \Delta u + f(u))|^2 dS \leq 0, \quad t \geq 0, \tag{3.25}$$

so the energy decays with time. On the other hand, one integrates (3.23) over S and derives the mass conservation:

$$\int_S u(\cdot, t) dS = \int_S u_0 dS, \quad t \geq 0. \tag{3.26}$$

Let τ be the time step size and let u^k be the approximation of u at $t_k = k\tau$ for $0 \leq k \leq [T/\tau]$ as before. The equation (3.23) with small ε presents some challenge for time discretization. Here, we use a second-order semi-implicit stabilizer scheme, which has proven to be quite stable for the phase model involving the Allen-Cahn equation even coupled with Navier-Stokes equations (see, e.g., [22], and refer to [51] for the error analysis). Such a scheme for (3.23) reads

$$\frac{3u^{k+1} - 4u^k + u^{k-1}}{2\tau} = \Delta \left(-\varepsilon^2 \Delta u^{k+1} + (2f(u^k) - f(u^{k-1})) + \lambda(u^{k+1} - 2u^k + u^{k-1}) \right), \tag{3.27}$$

where $\lambda > 0$ is a stabilizing parameter. Notice that the extra dissipative term $\lambda(u^{k+1} - 2u^k + u^{k-1})$ of order $\lambda\tau^2$ is added to improve the stability while preserving the simplicity of the semi-implicit scheme.

It is clear that the scheme (3.27) requires to solve biharmonic equations at each time step, which is troublesome for conforming spectral-element discretization. To overcome this, we introduce

$$w^{k+1} = -\varepsilon^2 \Delta u^{k+1} + (2f(u^k) - f(u^{k-1})) + \lambda(u^{k+1} - 2u^k + u^{k-1}), \tag{3.28}$$

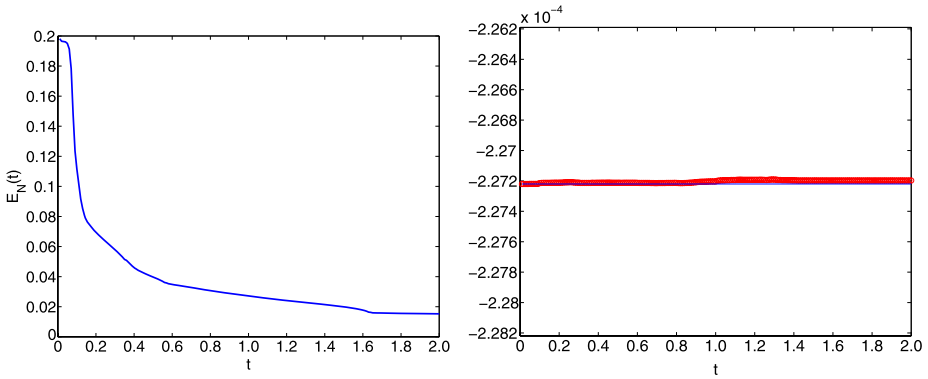


Fig. 10 Verification of (3.25) (left) and (3.26) (right) for $0 \leq t \leq 2$. Here, the parameters are the same as in Fig. 11

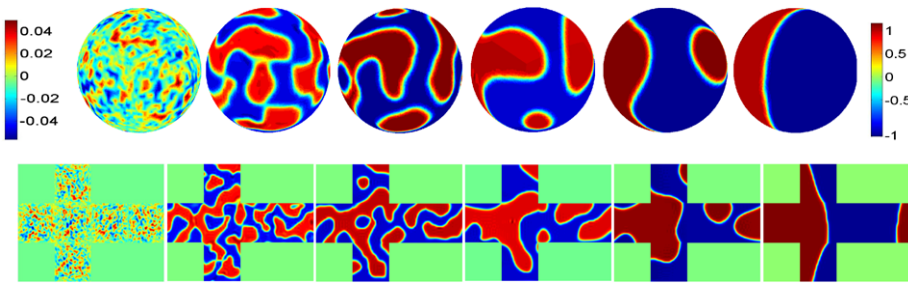


Fig. 11 Cahn-Hilliard equation for phase transition on the sphere obtained by the prolate-element method with $\varepsilon = 10^{-2}$, $\tau = 10^{-3}$, $N = 32$, $c = N/2$, and the initial value being zero mean perturbation of $u = 0$. The snapshots are taken at $t = 0, 0.2, 0.3, 0.5, 1, 1.7$

and rewrite (3.27) as a system of two second-order equations:

$$\begin{cases} 3u^{k+1} - 2\tau \Delta w^{k+1} = 4u^k - u^{k-1}, \\ -(\varepsilon^2 \Delta - \lambda)u^{k+1} - w^{k+1} = f(u^{k-1}) - 2f(u^k) + \lambda(2u^k - u^{k-1}). \end{cases} \tag{3.29}$$

Once again, at each time step, we need to solve elliptic equations as described in the first part of Sect. 3.3.

In the numerical tests, we take the initial value as a small perturbation of zero mean, i.e., $\int_S u_0 dS = 0$, and choose $\varepsilon = 10^{-2}$, $\tau = 10^{-3}$, $N = 32$ and $c = N/2$. We record in Fig. 10 the numerical energy E_N and the mass (the error $\max_k |\int_S u_N^k dS| = 2.94 \times 10^{-8}$), which verifies the property (3.25) and (3.26). It also shows that the proposed scheme is quite stable and accurate.

Several snapshots of the numerical solution are plotted in Fig. 11 on both S and the cube faces. We see that the disordered pattern quickly becomes well-organized and grouped, and the numerical solution separates the surface S into two regions S_+ and S_- , where it takes 1 and -1 , respectively, with a transition layer of width $O(\varepsilon)$. Due to the mass conservation (3.26), S_+ and S_- equally divides the sphere into two regions when the evolution reaches the steady state. Such a phase decomposition is typical in the planar domains and is also simulated in other geometries (cf. [15]).

Concluding Remarks In this paper, a p -type element method using the bandlimited PSWFs was proposed for solving various PDEs on the sphere. The partition of the sphere is based on a cubed-sphere transform, which is free of singularity. More importantly, the mapped prolate-Gauss-Lobatto points are almost uniformly distributed on the sphere, so the prolate-element method could significantly relax the constraint of explicit time stepping schemes for advection problems, and to increase the accuracy and enhance the spatial resolution for diffusion problems.

In the implementations, we merely decomposed the sphere into six patches (p -elements), but it is obvious that one can further partition each patch into many more elements. In this situation, the use of prolate-Gauss-Lobatto points must be more desirable than that based on the usual Legendre-Gauss-Lobatto points.

Appendix: Differential Operators in Curvilinear Coordinates

We start with the expressions of the most common differential operators such as gradient, divergence and Laplacian on the sphere in a general curvilinear coordinate (cf. [27, 30]). Let (X, Y, Z) be the Cartesian coordinate on the sphere S in (3.1), and let (α, β) be a curvilinear coordinate which could be one of the following coordinates:

- (i) (x, y) —the local coordinate on the cube faces in (3.2) obtained by the equidistant central projection;
- (ii) (ξ, η) —the coordinate of the reference square $\Lambda = [-1, 1]^2$ in (3.3) obtained by the equiangular central projection;
- (iii) (θ, ϕ) —the spherical coordinate in (3.5).

Let $\mathbf{r} = (X, Y, Z) = \mathbf{r}(\alpha, \beta)$. The covariant base vectors in (α, β) are defined by

$$\mathbf{a}_1 = \frac{\partial \mathbf{r}}{\partial \alpha}, \quad \mathbf{a}_2 = \frac{\partial \mathbf{r}}{\partial \beta}. \tag{A.1}$$

The metric tensor in (α, β) is

$$G = \begin{pmatrix} g_{11} & g_{12} \\ g_{21} & g_{22} \end{pmatrix} \quad \text{where } g_{ij} = \mathbf{a}_i \cdot \mathbf{a}_j, \quad i, j = 1, 2, \tag{A.2}$$

and denote its inverse by

$$G^{-1} = \begin{pmatrix} g^{11} & g^{12} \\ g^{21} & g^{22} \end{pmatrix} = \frac{1}{\det(G)} \begin{pmatrix} g_{22} & -g_{12} \\ -g_{12} & g_{11} \end{pmatrix}. \tag{A.3}$$

The contravariant base vectors are obtained by

$$\mathbf{a}^1 = g^{11} \mathbf{a}_1 + g^{12} \mathbf{a}_2, \quad \mathbf{a}^2 = g^{21} \mathbf{a}_1 + g^{22} \mathbf{a}_2. \tag{A.4}$$

Hence, a given vector \mathbf{v} in (α, β) can be expressed in both base vectors:

$$\mathbf{v} = v^1 \mathbf{a}_1 + v^2 \mathbf{a}_2 = v_1 \mathbf{a}^1 + v_2 \mathbf{a}^2. \tag{A.5}$$

Given a scalar field f , the gradient operator in the general curvilinear coordinates (α, β) is defined by

$$\nabla \equiv \frac{\partial}{\partial \alpha} \mathbf{a}^1 + \frac{\partial}{\partial \beta} \mathbf{a}^2, \quad \nabla f = \frac{\partial f}{\partial \alpha} \mathbf{a}^1 + \frac{\partial f}{\partial \beta} \mathbf{a}^2. \tag{A.6}$$

Let $g = \det(G)$, so \sqrt{g} is the Jacobian of the transform. We find from (A.5) and (A.6) that the divergence of a vector v in (A.5) is given by

$$\operatorname{div} v = \nabla \cdot v = \frac{1}{\sqrt{g}} \left(\frac{\partial}{\partial \alpha} (\sqrt{g} v^1) + \frac{\partial}{\partial \beta} (\sqrt{g} v^2) \right), \tag{A.7}$$

and

$$\begin{aligned} \Delta f &= \nabla \cdot (\nabla f) = \left(a^1 \frac{\partial}{\partial \alpha} + a^2 \frac{\partial}{\partial \beta} \right) \cdot \left(a^1 \frac{\partial f}{\partial \alpha} + a^2 \frac{\partial f}{\partial \beta} \right) \\ &= g^{11} \frac{\partial^2 f}{\partial \alpha^2} + g^{12} \frac{\partial^2 f}{\partial \alpha \partial \beta} + g^{21} \frac{\partial^2 f}{\partial \beta \partial \alpha} + g^{22} \frac{\partial^2 f}{\partial \beta^2} \\ &\quad + \left(a^1 \cdot \frac{\partial a^1}{\partial \alpha} + a^2 \cdot \frac{\partial a^1}{\partial \beta} \right) \frac{\partial f}{\partial \alpha} + \left(a^1 \cdot \frac{\partial a^2}{\partial \alpha} + a^2 \cdot \frac{\partial a^2}{\partial \beta} \right) \frac{\partial f}{\partial \beta}. \end{aligned} \tag{A.8}$$

Specifically, if (α, β) is one of the three coordinate systems of interest, it suffices to compute (A.1) or (A.2). For $(\alpha, \beta) = (x, y)$, we have

$$G = \frac{R^2}{r^4} \begin{pmatrix} a^2 + y^2 & -xy \\ -xy & a^2 + x^2 \end{pmatrix}, \quad r = \sqrt{a^2 + x^2 + y^2}. \tag{A.9}$$

For $(\alpha, \beta) = (\xi, \eta)$, the matrix tensor is given by

$$G = \frac{\pi^2 R^2}{16\rho^4} \sec^2 \left(\frac{\pi \xi}{4} \right) \sec^2 \left(\frac{\pi \eta}{4} \right) \begin{pmatrix} 1 + \tan^2 \left(\frac{\pi \xi}{4} \right) & -\tan \left(\frac{\pi \xi}{4} \right) \tan \left(\frac{\pi \eta}{4} \right) \\ -\tan \left(\frac{\pi \xi}{4} \right) \tan \left(\frac{\pi \eta}{4} \right) & 1 + \tan^2 \left(\frac{\pi \eta}{4} \right) \end{pmatrix}, \tag{A.10}$$

where

$$\rho = \sqrt{1 + \tan^2 \left(\frac{\pi \xi}{4} \right) + \tan^2 \left(\frac{\pi \eta}{4} \right)}.$$

The Jacobian of the transform is

$$\sqrt{g} = \sqrt{\det(G)} = \frac{\pi^2 R^2}{16\rho^3} \sec^2 \left(\frac{\pi \xi}{4} \right) \sec^2 \left(\frac{\pi \eta}{4} \right). \tag{A.11}$$

Notice that G is uniform for all six patches, so we can easily work out the differential operators (A.6)–(A.8) in (ξ, η) .

References

1. Al-Gwaiz, M.A.: *Sturm-Liouville Theory and Its Applications*. Springer, Berlin (2007)
2. Beylkin, G., Sandberg, K.: Wave propagation using bases for bandlimited functions. *Wave Motion* **41**(3), 263–291 (2005)
3. Boyd, J.P.: *Chebyshev and Fourier Spectral Methods*, 2nd edn. Dover, New York (2001)
4. Boyd, J.P.: Large mode number eigenvalues of the prolate spheroidal differential equation. *Appl. Math. Comput.* **145**(2), 881–886 (2003)
5. Boyd, J.P.: Prolate spheroidal wavefunctions as an alternative to Chebyshev and Legendre polynomials for spectral element and pseudospectral algorithms. *J. Comput. Phys.* **199**(2), 688–716 (2004)
6. Boyd, J.P.: Algorithm 840: computation of grid points, quadrature weights and derivatives for spectral element methods using prolate spheroidal wave functions-prolate elements. *ACM Trans. Math. Softw.* **31**(1), 149–165 (2005)

7. Cahn, J.W., Hilliard, J.E.: Free energy of a nonuniform system. I. Interface free energy. *J. Chem. Phys.* **28**(2), 258–267 (1958)
8. Canuto, C., Hussaini, M.Y., Quarteroni, A., Zang, T.A.: *Spectral Methods: Fundamentals in Single Domains*. Springer, Berlin (2006)
9. Canuto, C., Hussaini, M.Y., Quarteroni, A., Zang, T.A.: *Spectral Methods: Evolution to Complex Geometries and Applications to Fluid Dynamics*. Springer, Berlin (2007)
10. Chen, Q.Y., Gottlieb, D., Hesthaven, J.S.: Spectral methods based on prolate spheroidal wave functions for hyperbolic PDEs. *SIAM J. Numer. Anal.* **43**(5), 1912–1933 (2005)
11. Coddington, E.A., Levinson, N.: *Theory of Ordinary Differential Equations*. Tata McGraw-Hill, New Delhi (1972)
12. Deville, M.O., Fischer, P.F., Mund, E.H.: *High-order Methods for Incompressible Fluid Flow*. Cambridge University Press, Cambridge (2002)
13. Flammer, C.: *Spheroidal Wave Functions*. Stanford University Press, Stanford (1957)
14. Giraldo, F.X., Rosmond, T.E.: A scalable spectral element Eulerian atmospheric model (SEE-AM) for NWP: dynamical core tests. *Mon. Weather Rev.* **132**(1), 133–153 (2004)
15. Greer, J.B., Bertozzi, A.L., Sapiro, G.: Fourth order partial differential equations on general geometries. *J. Comput. Phys.* **216**(1), 216–246 (2006)
16. Hesthaven, J., Gottlieb, S., Gottlieb, D.: *Spectral Methods for Time-Dependent Problems*. Cambridge Monographs on Applied and Computational Mathematics. Cambridge University Press, Cambridge (2007)
17. Hundsdorfer, W.: *Numerical Solutions of Time-Dependent Advection-Diffusion-Reaction Equations*. Springer, Berlin (2007)
18. Iskandarani, M., Haidvogel, D.B., Boyd, J.P.: A staggered spectral element model with application to the oceanic shallow water equations. *Int. J. Numer. Methods Fluids* **20**(5), 393–414 (1995)
19. Kosloff, D., Tal-Ezer, H.: A modified Chebyshev pseudospectral method with an $O(N^{-1})$ time step restriction. *J. Comput. Phys.* **104**(2), 457–469 (1993)
20. Kovvali, N., Lin, W., Carin, L.: Pseudospectral method based on prolate spheroidal wave functions for frequency-domain electromagnetic simulations. *IEEE Trans. Antennas Propag.* **53**(12), 3990–4000 (2005)
21. Landau, H.J., Pollak, H.O.: Prolate spheroidal wave functions, Fourier analysis and uncertainty-III. The dimension of the space of essentially time- and band-limited signals. *Bell Syst. Tech. J.* **41**, 1295–1336 (1962)
22. Liu, C., Shen, J.: A phase field model for the mixture of two incompressible fluids and its approximation by a Fourier-spectral method. *Physica D* **179**(3–4), 211–228 (2003)
23. Loft, R.D., Thomas, S.J., Dennis, J.M.: Terascale spectral element dynamical core for atmospheric general circulation models. In: *Proceedings of the 2001 ACM/IEEE conference on Supercomputing (CDROM)*, p. 18. ACM, New York (2001)
24. McGregor, J.L.: Semi-Lagrangian advection on conformal-cubic grids. *Mon. Weather Rev.* **124**(6), 1311–1322 (1996)
25. Meixner, J., Schke, F.W.: *Mathiesche Funktionen und Sphroidfunktionen*. Springer, Berlin (1954)
26. Nair, R.D., Jablonowski, C.: Moving vortices on the sphere: A test case for horizontal advection problems. *Mon. Weather Rev.* **136**(2), 699–711 (2008)
27. Nair, R.D., Thomas, S.J., Loft, R.D.: A discontinuous Galerkin transport scheme on the cubed sphere. *Mon. Weather Rev.* **133**(4), 814–828 (2005)
28. Patera, A.T.: A spectral element method for fluid dynamics: laminar flow in a channel expansion. *J. Comput. Phys.* **54**(3), 468–488 (1984)
29. Phillips, N.A.: A coordinate system having some special advantages for numerical forecasting. *J. Atmos. Sci.* **14**(2), 184–185 (1957)
30. Prato, D.P.: Direct derivation of differential operators in curvilinear coordinates. *Am. J. Phys.* **45**, 1003 (1977)
31. Rancic, M., Purser, R.J., Mesinger, F.: A global shallow-water model using an expanded spherical cube: Gnomonic versus conformal coordinates. *Q. J. R. Meteorol. Soc.* **122**(532), 959–982 (1996)
32. Ronchi, C., Iacono, R., Paolucci, P.S.: The “cubed sphere”: a new method for the solution of partial differential equations in spherical geometry. *J. Comput. Phys.* **124**(1), 93–114 (1996)
33. Sadourny, R.: Conservative finite-difference approximations of the primitive equations on quasi-uniform spherical grids. *Mon. Weather Rev.* **100**(2), 136–144 (1972)
34. Sanderson, A.R., Kirby, R.M., Johnson, C.R., Yang, L.: Advanced reaction-diffusion models for texture synthesis. *J. Graph. GPU Game Tools* **11**(3), 47–71 (2006)
35. Schnakenberg, J.: Simple chemical reaction systems with limit cycle behaviour. *J. Theor. Biol.* **81**(3), 389–400 (1979)

36. Shen, J., Wang, L.L.: Error analysis for mapped Legendre spectral and pseudospectral methods. *SIAM J. Numer. Anal.* **42**(1), 326–349 (2005)
37. Shkolnisky, Y., Tygert, M., Rokhlin, V.: Approximation of bandlimited functions. *Appl. Comput. Harmon. Anal.* **21**(3), 413 (2006)
38. Slepian, D.: Prolate spheroidal wave functions, Fourier analysis and uncertainty-IV. Extensions to many dimensions; generalized prolate spheroidal functions. *Bell System Tech. J.* **43**, 3009–3057 (1964)
39. Slepian, D., Pollak, H.O.: Prolate spheroidal wave functions, Fourier analysis and uncertainty-I. *Bell Syst. Tech. J.* **40**, 43–63 (1961)
40. Taylor, M., Tribbia, J., Iskandarani, M.: The spectral element method for the shallow water equations on the sphere. *J. Comput. Phys.* **130**(1), 92–108 (1997)
41. Thomas, S.J., Loft, R.D.: Semi-implicit spectral element atmospheric model. *J. Sci. Comput.* **17**(1), 339–350 (2002)
42. Thomas, S.J., Dennis, J.M., Tufo, H.M., Fischer, P.F.: A Schwarz preconditioner for the cubed-sphere. *SIAM J. Sci. Comput.* **25**(2), 442–453 (2004)
43. Turing, A.M.: The chemical basis of morphogenesis. *Bull. Math. Biol.* **52**(1), 153–197 (1990)
44. Turk, G.: Generating textures on arbitrary surfaces using reaction-diffusion. In: *Proceedings of the 18th Annual Conference on Computer Graphics and Interactive Techniques*, p. 298. ACM, New York (1991)
45. Wang, L.L.: Analysis of spectral approximations using prolate spheroidal wave functions. *Math. Comput.* **79**(270), 807–827 (2010)
46. Witkin, A., Kass, M.: Reaction-diffusion textures. *ACM Siggraph Comput. Graph.* **25**(4), 299–308 (1991)
47. Wu, C., Deng, J., Chen, F.: Diffusion equations over arbitrary triangulated surfaces for filtering and texture applications. *IEEE Trans. Vis. Comput. Graph.* **14**(3), 666–679 (2008)
48. Xiao, H., Rokhlin, V., Yarvin, N.: Prolate spheroidal wavefunctions, quadrature and interpolation, Special issue to celebrate Pierre Sabatier’s 65th birthday (Montpellier). *Inverse Probl.* **17**(4), 805–838 (2000)
49. Yang, C., Cao, J., Cai, X.C.: A fully implicit domain decomposition algorithm for shallow water equations on the cubed-sphere. *SIAM J. Sci. Comput.* **32**(1), 418–438 (2010)
50. Yang, L., Zhabotinsky, A.M., Epstein, I.R.: Stable squares and other oscillatory Turing patterns in a reaction-diffusion model. *Phys. Rev. Lett.* **92**(19), 198303 (2004)
51. Yang, X.: Error analysis of a stabilized semi-implicit method for Allen-Cahn equation. *Discrete Contin. Dyn. Syst. Ser. B* **11**(4), 1057–1070 (2009)